POLITECNICO DI TORINO
Repository ISTITUZIONALE

On the (lack of) representativeness of quasi-static variational fracture models for unstable crack propagation

Original
On the (lack of) representativeness of quasi-static variational fracture models for unstable crack propagation / Chao Correas, A., Reinoso, J., Cornetti, P., Corrado, M.. - In: JOURNAL OF THE MECHANICS AND PHYSICS OF SOLIDS. - ISSN 0022-5096. - ELETTRONICO. - 186:(2024), pp. 1-20. [10.1016/j.jmps.2024.105573]

Availability:
This version is available at: 11583/2986343 since: 2024-02-26T08:35:51Z

Publisher:
Elsevier

Published
DOI:10.1016/j.jmps.2024.105573

Terms of use:

This article is made available under terms and conditions as specified in the corresponding bibliographic description in the repository

Publisher copyright

(Article begins on next page)

19 November 2026

J. Mech. Phys. Solids 186 (2024) 105573



Contents lists available at ScienceDirect

Journal of the Mechanics and Physics of Solids

journal homepage: www.elsevier.com/locate/jmps





On the (lack of) representativeness of quasi-static variational fracture models for unstable crack propagation

A. Chao Correas [a,b,*], J. Reinoso [b,c], P. Cornetti [a], M. Corrado [a]

[a] Department of Structural, Geotechnical and Building Engineering, Politecnico di Torino, Corso Duca degli Abruzzi 24, 10129 Turin, Italy
[b] Departamento de Mecánica de Medios Continuos y Teoría de Estructuras, ETS Ingeniería, Universidad de Sevilla, Camino de los Descubrimientos S/N, 41092 Seville, Spain
[c] ENGREEN - Laboratory of Engineering for Energy and Environmental Sustainability, Universidad de Sevilla, Seville, Spain

ARTICLE INFO

Keywords:
Phase field fracture model
Kinetic energy
Energetic barriers
3D printing
Experimental results
Dynamic fracture

ABSTRACT

The present work is devoted to prove that unstable crack propagation events do not comply with quasi-static hypotheses and thus should be modelled by dynamic approaches. Comprehensive supporting evidence is provided on the basis of three different analyses conducted on multi-ligament unstable fracture conditions, including a simplified Spring-Mass model, detailed quasi-static and dynamic Phase Field fracture models, and bespoke experiments with 3D printed specimens. The obtained results unequivocally show that neglecting the inertial effects can lead to unsafe predictions in the presence of energetic barriers for the development of fracture. Likewise, quasi-static Phase Field fracture models are proven to yield crack patterns that disagree with the experimental evidence because they overlook the progressive diffusion of the mechanical information within the continuum. Moreover, the inability of quasi-static approaches to follow unstable crack propagation is shown to weaken the crucial irreversibility condition of fracture. Overall, these experimentally backed insights should be gravely reckoned with, for they are not exclusive to Phase Field fracture models but common to (almost) any variational approach to fracture, *inter alia* Cohesive Zone Models or Continuum Damage Mechanics.

1. Introduction

Triggered by the work of Inglis (1913) on the singularities of linear elastic solutions at the tip of sharp cracks and corners, Griffith (1921) pioneered the energetic approach to fracture, i.e. the paradigm onto which the Fracture Mechanics field was later developed. His groundbreaking idea was to regard fracture initiation as a competition between the decrease of potential energy and increase of surface energy upon infinitesimal crack growth. This way, failure occurs whenever energetically favorable. Nonetheless, the simplicity of this rather fruitful approach entails some significant limitations. For instance, it is unable to describe how cracks nucleate and it only works when sufficiently large initial cracks are already present. Besides, the resulting predictions are limited to the loading intensity that triggers failure and to estimating the subsequent propagation stability and direction; complex crack patterns and fracture phenomena such as branching or coalescence are out of reach. On the other hand, relying on perfect linear elastic material behavior limits its applicability since real materials are not able to sustain infinite stress states. Eventually, excluding the kinetic energy variation from the energetic balance precludes it from properly assessing dynamic effects.

* Corresponding author.
E-mail address: arturo.chaocorreas@polito.it (A. Chao Correas).

https://doi.org/10.1016/j.jmps.2024.105573
Received 21 December 2023; Received in revised form 5 February 2024; Accepted 7 February 2024
Available online 9 February 2024
0022-5096/Â© 2024 The Authors. Published by Elsevier Ltd. This is an open access article under the CC BY license (http://creativecommons.org/licenses/by/4.0/).

Nomenclature

A	Imposed damage on $\partial_\alpha\Omega$
$\mathscr{A}$	Space-time action integral
$a(\alpha)$	Stiffness modulation function
B	Affine space of admissible damage fields
B_0	Evolution space of admissible damage variation fields
$\underline{b}$	Body forces
c	Speed of sound
c_w	Fracture energy scaling coefficient
E	Young's modulus
$\mathscr{E}_{\mathrm{frac}}$	Fracture energy functional
$\mathscr{E}_{\mathrm{str}}$	Strain energy functional
$\underline{f}$	Surface tractions
G	Potential energy release rate
G_C	Specific fracture energy
$\mathscr{K}$	Kinetic energy functional
$\mathscr{L}$	Generalized Lagrangian functional
ℓ	Internal length of the Phase Field fracture model
$\mathscr{P}$	Potential energy functional
t	Time
$\underline{U}$	Imposed displacement on $\partial_u\Omega$
$\underline{u}$	Displacement vector field
$\underline{\dot{u}}$	Velocity vector field
$\underline{\ddot{u}}$	Acceleration vector field
V	Affine space of admissible displacement fields
V_0	Evolution space of admissible displacement variation fields
$\mathscr{W}_{\mathrm{ext}}$	External work functional
$w(\alpha)$	Local fracture energy function
$\underline{x}$	Spatial coordinates
α	Damage field/Phase field
Γ	Internal sharp crack set
$\delta\alpha$	Damage variation field
$\delta\underline{u}$	Displacement variation field
$\underline{\underline{\varepsilon}}$	Infinitesimal strain tensor field
λ, μ	Lamé constants
ν	Poisson's ratio
ρ	Mass density
$\underline{\underline{\sigma}}$	Stress tensor field
σ_C	Tensile strength
ψ	Strain energy density function
Ω	Structural domain
$\partial\Omega$	External boundary of Ω
$\partial_u\Omega$	Dirichlet boundary of Ω for the displacement problem
$\partial_f\Omega$	Neumann boundary of Ω for the displacement/acceleration problem
$\partial_\alpha\Omega$	Dirichlet boundary of Ω for the phase field problem

In the aim of introducing a new framework retaining the strengths of Griffith's energetic approach while keeping stresses finite, Dugdale (1960) and Barenblatt (1962) introduced the concept of cohesive forces. Their proposal was conceptually simple yet backed by the essence of intermolecular forces: the stress-strain constitutive relation of a continuum is only valid below a certain stress threshold, above which the behavior turns cohesive. This means that a process zone appears in the surroundings of intense stress concentrators so as to accommodate material softening therein. Likewise, the methodology can be approached variationally, resulting in manageable numerical implementation and easiness in incorporating the kinetic energy component. Consequently, cohesive models were utilized for studying fracture in a wide range of dynamic conditions, inter alia high-velocity impacts (Camacho and Ortiz, 1996), shattering of tempered glass panes (Vocialta et al., 2018), and unstable crack propagations (Laschuetza and Seelig, 2021; Vieira de Carvalho et al., 2024). However, such numerical models allow crack development in predefined locations due to the interfacial nature of cohesive behavior, thus limiting its suitability for representing bulk fracture.

To cover said niche, Francfort and Marigo (1998) revisited Griffith's approach to brittle bulk fracture from a variational

perspective. This was followed by Bourdin et al. (2000) who, based on the works by Ambrosio and Tortorelli (1990) in the field of image segmentation, put forward a convenient and mathematically rigorous regularization enabling numerical resolution. The resultant variational framework, known as the Phase Field fracture model (PFM), proved theoretically robust and able to predict both crack nucleation and complex cracking without any *a priori* considerations or additional ad-hoc criteria. This, combined with a rather straightforward numerical implementation, has made the approach very popular within the computational Fracture Mechanics community.

Although it was conceptualized for quasi-static setups (see e.g. Bourdin et al., 2008 and Miehe et al., 2010a), many studies introducing the kinetic energy component in the PFM formulation have been conducted. In this regard, one can identify the complementary works of Larsen et al. (2010) and Bourdin et al. (2011) as a starting point: the former proved that the latter's time-discretized approach, which couples elastodynamics and PFM, converges to the continuous solution and fulfils the total energy balance as the step size vanishes. Striving for a more algorithmically convenient approach instead, Borden et al. (2012) and Hofacker and Miehe (2013) proposed similar dynamic PFM frameworks, in which the governing principles were derived from the Euler-Lagrange equation and a damage history variable was used to strongly impose the irreversibility condition. Another somewhat heuristic approach to the dynamic PFM was presented by Schlüter et al. (2014) on the basis of Hamilton's principle. Therein, the irreversibility condition was tackled through the updating of Dirichlet boundary conditions on the damage field wherever it reached a certain threshold. Back to rigorous formalisms, a framework that considers the irreversibility condition through variational inequalities in the context of Hamilton's principle was initially presented by Li et al. (2015) and further developed by Li et al. (2016). Thereafter, several studies were devoted to assess the PFM's predictive capabilities for dynamic fracture phenomena, such as microbranching (Bleyer and Molinari, 2017), crack tip velocity evolution (Bleyer et al., 2017), dynamic fracturing of hyperelastic materials (Tian et al., 2020), and interaction between dynamic bulk fracture and cohesive interfaces (Corrado et al., 2022), to mention but a few.

Given that both quasi-static and dynamic PFM frameworks are well-established, it is natural to compare the resultant predictions upon the "grey area" conditions of unstable crack propagation under quasi-static loadings. Scenarios where energetic barriers for crack growth are present result of particular interest. In such regard, this work drew inspiration primarily from three sources: (i) the empirical evidence provided by Zhou (1996) on the strong dynamic nature of unstable crack propagation under globally quasi-static conditions; (ii) the experimentally observed effect of energetic barriers on the development of cracks (Albertini et al., 2021); and (iii) the feasibility of engineering crack patterns through the placement of interacting stress concentrators (Cavuoto et al., 2022). Theoretical and experimental results are presented to show that dynamic effects play an important role in unstable crack propagation events. This directly contravenes the fundamental hypothesis of quasi-static fracture models, making them unsuitable for such conditions. More importantly, the resultant quasi-static predictions are potentially unsafe in addition to being conceptually flawed.

2. Quasi-static variational approach to bulk fracture

Let us consider the quasi-static Fracture Mechanics problem depicted in Fig. 1, in which a structural domain $\Omega \subset \mathbb{R}^N | N \in \{2,\ 3\}$ with an external boundary $\partial\Omega \subset \mathbb{R}^{N-1}$ is filled with a homogeneous, isotropic, linear elastic and brittle material, whose elastic and ultimate behaviors are governed by the Lamé constants λ and μ, and by the specific fracture energy G_C. Furthermore, let us introduce an internal sharp crack $\Gamma \subset \mathbb{R}^{N-1}$ in the solid domain Ω, so that the displacement field $\underline{u}$ is no longer necessarily continuous along Γ, yet it satisfies Dirichlet and homogeneous Neumann boundary conditions on $\partial_u\Omega$ and $\partial_f\Omega = \partial\Omega \setminus \partial_u\Omega$, respectively. Moreover, Ω is not subjected to any distributed body forces $\underline{b}$ and thus the work done by external prescribed forces $\mathscr{W}_{\text{ext}}$ is null. In these conditions, the potential energy of the system $\mathscr{P}$ at each "instant" t gets defined as a sum of the strain energy $\mathscr{E}_{\text{str}}$ and the fracture energy $\mathscr{E}_{\text{frac}}$, in turn defined

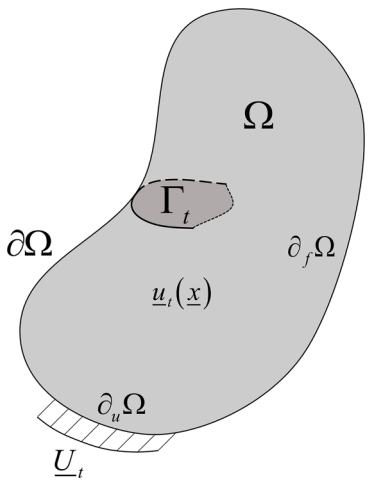


Fig. 1. Schematic representation of a classical quasi-static Fracture Mechanics problem.

as:

$$\mathscr{P}\left(\underline{u}_t,\ \Gamma_t\right) = \mathscr{E}_{\text{str}}\left(\underline{u}_t,\ \Gamma_t\right) + \mathscr{E}_{\text{frac}}(\Gamma_t), \tag{1}$$

$$\mathscr{E}_{\text{str}}\left(\underline{u}_t,\ \Gamma_t\right) = \int_{\Omega\setminus\Gamma_t} \frac{1}{2}\lambda \text{tr}\left(\underline{\underline{\varepsilon}}\left(\underline{u}_t\right)\right)^2 + \mu\left(\underline{\underline{\varepsilon}}\left(\underline{u}_t\right) : \underline{\underline{\varepsilon}}\left(\underline{u}_t\right)\right) \mathrm{d}\underline{x}, \tag{2}$$

$$\mathscr{E}_{\text{frac}}(\Gamma_t) = \int_{\Gamma_t} G_C \,\mathrm{d}\underline{x}, \tag{3}$$

where the notation $(\bullet)_t$ stands for $(\bullet)$ at the "instant" t, the underline indicates a vector field, the double underline a tensor field, and $\underline{\underline{\varepsilon}}\left(\underline{u}\right)$ is the conventional infinitesimal strain tensor:

$$\underline{\underline{\varepsilon}}\left(\underline{u}\right) = \frac{\nabla\underline{u} + \nabla^{\mathrm{T}}\underline{u}}{2}. \tag{4}$$

Now, the variational approach to bulk fracture introduced by Francfort and Marigo (1998) posits that the system evolves following the states $\left(\underline{u}_t,\ \Gamma_t\right)$ that globally minimize the potential energy $\mathscr{P}$. To avoid unrealistic material healing, Γ_t is constrained by an irreversibility condition so that $\Gamma_t \subseteq \Gamma_{t+\Delta t}$ for $\Delta t > 0$. Thereby, Γ cannot shrink nor translate with respect to previous states, but it can remain as-is, grow from an existing crack or nucleate a new one. Considering non-null external forces, of either body or surface type, can jeopardize the postulate of minimization of potential energy in the considered quasi-static setup due to domain softening as the crack grows (Francfort and Marigo, 1998).

Clearly, the minimization of potential energy implies that Γ can only grow whenever the loss of $\mathscr{E}_{\text{str}}$ at least suffices the increase of $\mathscr{E}_{\text{frac}}$, it being otherwise energetically too expensive. Likewise, resultant crack patterns upon growth are those globally minimizing $\mathscr{P}$, hence complex cracking phenomena such as branching, coalescence or kinking are inherently considered without further ad-hoc criteria.

Despite the many strengths and intuitiveness of the approach, the original proposal by Francfort and Marigo (1998) is not devoid of problems. For instance, it relies on the global minimization of the system's potential energy, a questionable assumption that allows the system to overcome any arbitrarily large energetic barrier in order to reach the globally stable state (Negri and Ortner, 2008). Besides, the numerical implementation of the approach is rather arduous since $\underline{u}$ is generally discontinuous along Γ, which in turn is time dependent and not necessarily conforming with the spatial discretization of Ω.

To render the variational approach numerically manageable, Bourdin et al. (2000) proposed a regularized approach inspired by previous works of Ambrosio and Tortorelli (1990) in the field of image segmentation. This consisted in introducing one extra continuous scalar field to the displacement problem, the so-called *phase field* α, which governs the transition from pristine $(\alpha = 0)$ to broken $(\alpha = 1)$ conditions with ℓ as a regularization length. Consequently, the sharp discontinuities of $\underline{u}$ along Γ get smeared into the domain Ω, thus ensuring that $\underline{u}$ remains continuous even in "cracked" domains. At the same time, a proper elliptic functional of α was introduced to approximate the surface integral in $\mathscr{E}_{\text{frac}}$ by a domain integral. The regularized variational problem originally proposed by Bourdin et al. (2000) can be interpreted as the global minimization of a functional $\mathscr{P}$ defined as follows:

$$\mathscr{P}\left(\underline{u}_t,\ \alpha_t\right) = \mathscr{E}_{\text{str}}\left(\underline{u}_t,\ \alpha_t\right) + \mathscr{E}_{\text{frac}}(\alpha_t), \tag{5}$$

$$\mathscr{E}_{\text{str}}\left(\underline{u}_t,\ \alpha_t\right) = \int_{\Omega}\left[(1-\alpha_t)^2 + k\right]\left[\frac{1}{2}\lambda \text{tr}\left(\underline{\underline{\varepsilon}}\left(\underline{u}_t\right)\right)^2 + \mu\left(\underline{\underline{\varepsilon}}\left(\underline{u}_t\right) : \underline{\underline{\varepsilon}}\left(\underline{u}_t\right)\right)\right] \mathrm{d}\underline{x}, \tag{6}$$

$$\mathscr{E}_{\text{frac}}(\alpha_t) = \int_{\Omega} G_C\left[\frac{\alpha_t^2}{2\ell} + \frac{\ell}{2}(\nabla\alpha_t \cdot \nabla\alpha_t)\right] \mathrm{d}\underline{x}, \tag{7}$$

where k represents a small parameter $(k \ll 1)$ used to avoid ill-posedness of the numerical problem as $\alpha \to 1$. Clearly, for $\underline{u}_t$ and α_t to be admissible solutions of the minimization, both fields must comply with their corresponding Dirichlet boundary conditions, i.e. $\underline{u}_t\left(\underline{x} \in \partial_u\Omega\right) = \underline{U}_t$ and $\alpha_t\left(\underline{x} \in \partial_\alpha\Omega\right) = A_t$. Likewise, α_t is also subjected to an irreversibility condition along the whole domain Ω such that $\alpha_t \geq \alpha_s\ \forall\ s < t$, so as to forbid unphysical material healing.

On the downside, the regularized energy functional $\mathscr{P}$ is not convex in $\left(\underline{u},\ \alpha\right)$, thus hindering the obtention of global minimizers. Still, alternate minimization (AltMin) algorithms can be easily implemented in numerical platforms since $\mathscr{P}$ is convex in both $\left(\underline{u};\ \alpha\right)$

and $\left(\alpha;\, \underline{u}\right)$, where the semicolon separates variable fields on the left from fixed ones on the right. However, this staggered and iterative technique only converges to stationary points and not to global minimizers (Sargado et al., 2018). In any case, metastable evolutions are probably more realistic than globally stable ones, as already suggested by Bourdin et al. (2000). This, combined with its proven thermodynamical consistency (Miehe et al., 2010), made the AltMin scheme the default implementation for the PFM (see e.g. Bourdin et al., 2008, Miehe et al., 2010a and Marigo et al., 2016). Relaxing the search of minimizers from global to local also realigns the variational approach to fracture with the conventional Griffith criterion for crack propagation (Griffith, 1921). This reconciliation also includes inheriting one of the latter's main drawbacks: the unphysical energy losses upon unstable crack propagation (Sargado et al., 2018). In this regard, it was already pointed out by Negri and Ortner (2008) that these events are dynamic in nature, and so the actual energetic transformations cannot be captured by quasi-static approaches. In what follows, several theoretical analyses, backed by experimental results, are presented to support such a bold statement.

3. Equivalent spring-mass model of unstable crack propagation

Crack propagation is defined as unstable when it becomes self-sustained once triggered, meaning that the release rate of potential energy stored in the domain exceeds the specific increase of fracture energy due to the new cracks. Using Griffith's conventional notation, a crack propagates unstably after nucleation when $\partial G/\partial\Gamma > \partial G_C/\partial\Gamma$, G being the potential energy release rate. These fracturing events develop abruptly over short periods of time in which the system's mechanical configuration noticeably changes, thus being essentially a dynamic problem. As a consequence, neither the system's kinetic energy nor its contribution to crack propagation are negligible, which directly contravenes the basic requisites of quasi-static modelling.

In order to illustrate the generalities of this issue, let us now consider the setup in Fig. 2(a) where a generic 2D linear elastic and perfectly brittle domain under uniaxial tension presents a resisting section composed of two ligaments of different overall strength. In such a case, a first order approximation of the system's overall mechanical response can be obtained through the single degree-of-freedom spring-mass model in Fig. 2(b).

Given the domain's layout and boundary conditions, fracture is restricted to develop unstably within each of the two ligaments. The elongation and ultimate behavior of the i-th ligament ($i = \{1, 2\}$) can be then approximated by a linear spring of pristine stiffness K_i with a cut-off at $z = z_{Ci} > 0$ as in Eq. (8), the loss of stiffness being irrevocable.

$$K_i(z) = \begin{cases} K_i & \text{for} \quad z < z_{Ci} \\ 0 & \text{for} \quad z \geq z_{Ci} \end{cases} \tag{8}$$

For the sake of simplicity and with little loss of generality, two further hypotheses are introduced: (i) U_t monotonically and quasi-statically increases with time; (ii) the ligament 1 is weaker, and so z_{C1} and z_{C2} follow Eq. (9) with z_{C1} and Δz_C strictly positive.

$$z_{C2} = z_{C1} + \Delta z_C \tag{9}$$

In such conditions, the system's degree of freedom z_t evolves following quasi-static equilibrium states $\widetilde{z}_t$ up to the breakage of spring 1, which by convention occurs at $t = 0$ so that $z_{t=0} = z_{C1}$. In order to ensure that no extra energy is introduced in the system thereafter, U_t gets frozen at its value at $t = 0$. Mathematically, these two statements read as:

$$z_t = \widetilde{z}_t = \frac{K}{K + K_1 + K_2} U_t \quad \text{for} \quad t < 0, \tag{10}$$

$$U_t = U_{C1} = \frac{K + K_1 + K_2}{K} z_{C1} \quad \text{for} \quad t \geq 0. \tag{11}$$

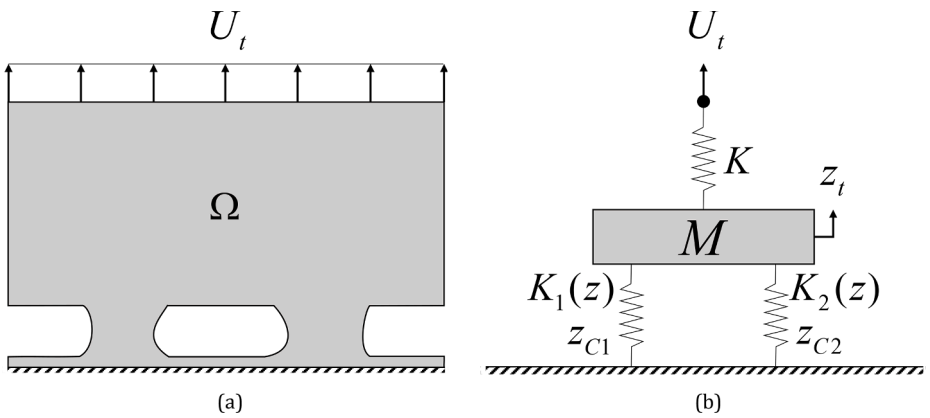


Fig. 2. Schematic representation of: (a) a domain with two resisting ligaments that features unstable crack propagation, and (b) its equivalent spring mass model.

Once the spring 1 snaps at $t = 0$, both the system's mechanical configuration and its position of quasi-static equilibrium $\widetilde{z}_t$ change suddenly. This means that the system is no longer in quasi-static equilibrium of forces for $t \geq 0$, and that dynamic evolution takes place instead. In this sense, such dynamic motion is governed by the following well-known initial value problem (valid up to the failure of the spring 2, should it happen):

$$\begin{cases} M\,\ddot{z}_t + (K + K_2) z_t = (K + K_1 + K_2)\, z_{C1} \\ z_0 = z_{C1} \\ \dot{z}_0 = 0 \end{cases} \quad \text{for} \quad t \geq 0, \tag{12}$$

which can be solved analytically, yielding the subsequent temporal law for z_t:

$$z_t = [C_0 - C_1 \cos(\omega_0 t)] z_{C1} \quad \text{for} \quad t \geq 0, \tag{13}$$

where:

$$C_0 = \frac{K + K_1 + K_2}{K + K_2}, \quad C_1 = \frac{K_1}{K + K_2}, \tag{14}$$

and ω_0 stands for the system's natural frequency:

$$\omega_0 = \sqrt{\frac{K + K_2}{M}}. \tag{15}$$

Therefore, at $t = 0$ the system initiates a harmonic oscillation of amplitude $2C_1 z_{C1}$ and period $2\pi\omega_0$, centered at the new quasi-static equilibrium state $\widetilde{z}_{t\geq 0} = C_0 z_{C1}$. Neglecting the inertial effects would thus yield unsafe predictions in which the maximum tensile deformation reached by spring 2 is underestimated. In particular, should C_0, C_1, z_{C1} and Δz_C be so that $C_0 z_{C1} < z_{C1} + \Delta z_C \leq (C_0 + C_1) z_{C1}$, quasi-static predictions would foresee the spring 2 not reaching its critical elongation as opposed to what is predicted dynamically.

This difference can be easily understood when looking at the problem from an energetic perspective. In the quasi-static approach, the system seeks the minimization of the deformation energy by instantaneously following the states of quasi-static equilibrium $\widetilde{z}_t$. This is done with no regard to the temporal continuity of z_t or to the energetic conservativeness of the system. In reality, these two aspects play a pivotal role in the evolution of massive systems. Indeed, once spring 1 breaks, its deformation energy is immediately lost, but the system is still in excess of deformation energy with respect to the new quasi-static equilibrium state since $z_{t=0} = z_{C1} \neq \widetilde{z}_{t\geq 0} = C_0 z_{C1}$. This surplus of energy drives an oscillatory motion, which is the manifestation of cyclic and reversible transformations of deformation energy to kinetic and vice versa.

Moreover, these transformations take place continuously in time and are governed by the system natural frequency ω_0, and so no reaction to changes in the system's configuration is immediate. Generalizing to a continuum, this results in the mechanical information diffusing at a finite, material-dependent velocity, namely the speed of sound c. In quasi-static frameworks, this physical constraint is completely overlooked by assuming that both the system reactions and the propagation of mechanical information are instantaneous. Particularly, this simplification is expected to have a noticeable disruptive effect on unstable fracturing, given that the crack tip velocity is often of the same order of magnitude as the speed of sound.

4. Theoretical framework of the dynamic Phase Field fracture model

Let us now recall the conventional quasi-static PFM approach introduced in Section 2 and develop the generalization, as presented by Li et al. (2016), to a dynamic context where inertial effects are significant. Therefore, in addition to the properties and parameters already defined, i.e. E, ν, G_C and ℓ, the material mass density ρ is also required. Furthermore, setting up a dynamic framework reinstates the physical meaning of t as a temporal variable that directly intervenes in the formulation; hence, it is no longer just an identifier of the different resolution steps as in the quasi-static case. The kinetic $\mathscr{K}$, strain $\mathscr{E}_{\text{str}}$ and fracture $\mathscr{E}_{\text{frac}}$ energy components, as well as the work done by the prescribed external forces $\mathscr{W}_{\text{ext}}$, can be then defined as follows:

$$\mathscr{K}\left(\underline{\dot{u}}_t,\ t\right) = \frac{1}{2}\int_\Omega \rho\, \underline{\dot{u}}_t \cdot \underline{\dot{u}}_t \, \mathrm{d}\underline{x}, \tag{16}$$

$$\mathscr{E}_{\text{str}}\left(\underline{u}_t,\ \alpha_t,\ t\right) = \int_\Omega \psi\left(\underline{\underline{\varepsilon}}\left(\underline{u}_t\right),\ a(\alpha_t)\right) \mathrm{d}\underline{x}, \tag{17}$$

$$\mathscr{E}_{\text{frac}}(\alpha_t,\ t) = \int_\Omega \frac{G_C}{c_w}\left[\frac{w(\alpha_t)}{\ell} + \ell(\nabla\alpha_t \cdot \nabla\alpha_t)\right] \mathrm{d}\underline{x}, \tag{18}$$

$$\mathscr{W}_{\text{ext}}\left(\underline{u}_t,\ t\right) = \int_\Omega \underline{b}_t \cdot \underline{u}_t \, \mathrm{d}\underline{x} + \int_{\partial_f\Omega} \underline{f}_t \cdot \underline{u}_t \, \mathrm{d}\underline{x}, \tag{19}$$

where $\underline{\dot{u}}$ represents the velocity field, ψ is the strain energy density modulated by a function a of α, w is a function governing the local term of $\mathscr{E}_{\text{frac}}$, c_w is a scaling parameter defined as in Eq. (20) (Marigo et al., 2016), and $\underline{b}$ and $\underline{f}$ represent the prescribed body forces and surface tractions, respectively. The particular definition of the functions ψ, a and w has been the subject of extensive research and many options have been proposed in the literature (see e.g. Pham et al., 2011, Marigo et al., 2016, Wu 2017 and De Lorenzis and Maurini 2022), each choice yielding a different fracture behavior.

$$c_w = 4\int_0^1 \sqrt{w(\zeta)}\,\mathrm{d}\zeta \tag{20}$$

For the variational setup at hand, both the motion and damage problems are subjected to Dirichlet boundary conditions along $\partial_u\Omega$ and $\partial_\alpha\Omega$, respectively. As a consequence, $\underline{u}_t$ and α_t fields are admissible for every instant t of the evolution if they belong to the corresponding affine spaces V_t and B_t defined in Eqs. (21) and (22). Clearly, given that $\underline{\dot{u}} = \mathrm{d}\underline{u}/\mathrm{d}t$ and $\underline{\ddot{u}} = \mathrm{d}^2\underline{u}/\mathrm{d}t^2$, the admissibility of the velocity and acceleration fields does not need to be imposed from a theoretical point of view, for it is an outcome of the admissibility of the corresponding displacement field.

$$\mathrm{V}_t = \left\{ \underline{u}_t \;:\; \Omega \to \mathbb{R}^N \;\middle|\; \underline{u}_t = \underline{U}_t \quad \forall \underline{x} \in \partial_u\Omega \right\} \tag{21}$$

$$\mathrm{B}_t = \left\{ \alpha_t \;:\; \Omega \to [0,1] \;\middle|\; \begin{array}{ll} \alpha_t = A_t & \forall \underline{x} \in \partial_\alpha\Omega \quad \text{and} \\ 0 \le \alpha_\tau \le \alpha_t \le 1 & \forall \underline{x} \times \tau \in \Omega \times [0,t) \end{array} \right\} \tag{22}$$

Furthermore, the governing Hamilton's principle requires that, for any evolution in time of the irreversibly conditioned system within the time interval $T = [0,\ t']$, the admissible displacement and damage variations, namely $\delta\underline{u}$ and $\delta\alpha$, are those belonging to the respective evolution spaces V_0 and B_0 from Eqs. (23) and (24). Note that ∂T stands for the extremes of T, i.e. $t = \{0,\ t'\}$.

$$\mathrm{V}_0 = \left\{ \delta\underline{u} \;:\; \Omega \times T \to \mathbb{R}^N \;\middle|\; \begin{array}{ll} \delta\underline{u} = \underline{0} & \forall \underline{x} \times t \in \partial_u\Omega \times T \quad \text{and} \\ \delta\underline{u} = \underline{0} & \forall \underline{x} \times t \in \Omega \times \partial T \end{array} \right\} \tag{23}$$

$$\mathrm{B}_0 = \left\{ \delta\alpha \;:\; \Omega \times T \to [0,1] \;\middle|\; \begin{array}{lll} \delta\alpha = 0 & \forall \underline{x} \times t \in \partial_\alpha\Omega \times T & \text{and} \\ \delta\alpha = 0 & \forall \underline{x} \times t \in \Omega \times \partial T & \text{and} \\ 0 \le \alpha_\tau \le \alpha_t + \delta\alpha \le 1 & \forall \underline{x} \times \tau \in \Omega \times [0,\ t) & \end{array} \right\} \tag{24}$$

The system's energy components in Eqs. (16) to (19) can be combined to obtain a generalized Lagrangian functional $\mathscr{L}$ per Eq. (25), which once integrated over the time interval T, yields the space-time action integral $\mathscr{A}$ defined in Eq. (26).

$$\mathscr{L}\left(\underline{u}_t,\ \underline{\dot{u}}_t,\ \alpha_t,\ t\right) = -\mathscr{K}\left(\underline{\dot{u}}_t,\ t\right) + \mathscr{E}_{\text{str}}\left(\underline{u}_t,\ \alpha_t,\ t\right) + \mathscr{E}_{\text{frac}}(\alpha_t,\ t) - \mathscr{W}_{\text{ext}}\left(\underline{u}_t,\ t\right) \tag{25}$$

$$\mathscr{A}\left(\underline{u}_t,\ \underline{\dot{u}}_t,\ \alpha_t,\ t'\right) = \int_0^{t'} \mathscr{L}\left(\underline{u}_\tau,\ \underline{\dot{u}}_\tau,\ \alpha_\tau,\ t\right)\mathrm{d}t \tag{26}$$

According to Hamilton's principle, a system with state variables subjected to inequality constraints (as the one here at hand) will evolve in time following the states $\left(\underline{u}_t,\ \underline{\dot{u}}_t,\ \alpha_t\right)$ so that, upon any combination of the admissible motion and damage variations $\left(\delta\underline{u},\ \delta\alpha\right)$, it holds that $\delta\mathscr{A} \ge 0$. Developing this variational principle, performing some algebraic manipulations, and considering that it must hold $\forall t' \ge 0$, the resulting generalized Euler-Lagrange equation governing the evolution in time of the system reads:

$$-\frac{\mathrm{d}}{\mathrm{d}t}\left(\mathrm{D}_{\underline{\dot{u}}}\mathscr{L}\left(\underline{u}_t,\ \underline{\dot{u}}_t,\ \alpha_t,\ t\right)\right)\left[\delta\underline{u}\right] + \mathrm{D}_{\underline{u}}\mathscr{L}\left(\underline{u}_t,\ \underline{\dot{u}}_t,\ \alpha_t,\ t\right)\left[\delta\underline{u}\right] + \mathrm{D}_{\alpha}\mathscr{L}\left(\underline{u}_t,\ \underline{\dot{u}}_t,\ \alpha_t,\ t\right)[\delta\alpha] \ge 0 \quad \forall\left\{\delta\underline{u},\ \delta\alpha\right\} \in \{\mathrm{V}_0, \mathrm{B}_0\}, \tag{27}$$

where $\mathrm{D}_\phi\mathscr{F}(\phi,\ldots)[\delta\phi]$ stands for the first Gateaux derivative of the functional $\mathscr{F}(\phi,\ldots)$ with respect to ϕ and in the direction of $\delta\phi$.

The concept behind Eq. (27) is straightforward: the dynamic system evolves in time following the path of kinematically admissible states that yield first-order stationarity of $\mathscr{A}$ ($\delta\mathscr{A} = 0$) as long as they do not violate the irreversibility condition, in which case the first variation of the action is ought to be positive ($\delta\mathscr{A} > 0$). However, since solving such variational principle in a monolithic manner can result rather tortuous, it is often resolved through a staggered approach. This results in two more easily solvable governing principles that read:

$$-\frac{\mathrm{d}}{\mathrm{d}t}\left(\mathrm{D}_{\underline{\dot{u}}}\mathscr{L}\left(\underline{u}_t,\ \underline{\dot{u}}_t,\ t;\ \alpha\right)\right)\left[\delta\underline{u}\right] + \mathrm{D}_{\underline{u}}\mathscr{L}\left(\underline{u}_t,\ \underline{\dot{u}}_t,\ t;\ \alpha\right)\left[\delta\underline{u}\right] = 0 \quad \forall\,\delta\underline{u} \in \mathrm{V}_0, \tag{28}$$

$$\mathrm{D}_{\alpha}\mathscr{I}\left(\alpha_t,\ t;\ \underline{u},\ \dot{\underline{u}}\right)[\delta\alpha] \geq 0 \quad \forall\, \delta\alpha \in \mathrm{B}_0. \tag{29}$$

Eq. (28) imposes the system to be in dynamic equilibrium for a given fixed damage field, while Eq. (29) governs damage evolution for a certain state of motion. In each case, the fixed parameters fed to each equation should correspond to the respective best available guesses. However, the straightforward resolution of first Eq. (28) and then Eq. (29), or vice versa, does not necessarily yield a good approximation to the solution of Eq. (27), especially when large time increments between steps are used. For this reason, staggered approaches are commonly coupled with AltMin schemes, in which the resolution of both the motion and damage problems is iterated back and forth until a certain convergence criterion is met, and the problem resolution can proceed to the next time step.

Eventually, considering the particular definition of the energy components in Eqs. (16) to (19) and developing the derivatives in Eqs. (28) and (29), one obtains:

$$\int_{\Omega} \rho\ddot{\underline{u}}_t \cdot \delta\underline{u}\ \mathrm{d}\underline{x} + \int_{\Omega} \underline{\underline{\sigma}}\left(\underline{\underline{\varepsilon}}\left(\underline{u}_t\right);\ \alpha\right) : \underline{\underline{\varepsilon}}\left(\delta\underline{u}\right)\ \mathrm{d}\underline{x} = \int_{\Omega} \underline{b}_t \cdot \delta\underline{u}\ \mathrm{d}\underline{x} + \int_{\partial_f\Omega} \underline{f}_t \cdot \delta\underline{u}\ \mathrm{d}\underline{x} \quad \forall \delta\underline{u} \in \mathrm{V}_0, \tag{30}$$

$$\int_{\Omega} \frac{G_C}{c_w}\left[\frac{w'(\alpha_t)}{\ell} \cdot \delta\alpha + 2\ell(\nabla\alpha_t \cdot \nabla\delta\alpha)\right]\ \mathrm{d}\underline{x} + \int_{\Omega} \frac{\partial\psi\left(\alpha_t;\ \underline{\underline{\varepsilon}}\left(\underline{u}\right)\right)}{\partial\alpha} \cdot \delta\alpha\ \mathrm{d}\underline{x} \geq 0 \quad \forall\delta\alpha \in \mathrm{B}_0 \tag{31}$$

where $\underline{\underline{\sigma}}$ stands for the stress field, defined as the dual magnitude of the strain tensor (see Eq. (32)), and $w'(\alpha)$ indicates the first function derivative of w with respect to α.

$$\underline{\underline{\sigma}}\left(\underline{\underline{\varepsilon}}\left(\underline{u}\right);\ \alpha\right) = \frac{\partial\psi\left(\underline{\underline{\varepsilon}}\left(\underline{u}\right);\ \alpha\right)}{\partial\underline{\underline{\varepsilon}}} \tag{32}$$

Therefore, there exists three different unknown fields in the two variational principles, namely the displacement $\underline{u}$ and acceleration $\ddot{\underline{u}}$ fields in the motion principle, plus the damage field α in the homonym principle. Since monolithic resolution of Eq. (30) in terms of $\left(\ddot{\underline{u}},\ \underline{u}\right)$ is not straightforward, time integrators are usually implemented to provide relations between $\underline{u}$, $\dot{\underline{u}}$ and $\ddot{\underline{u}}$, eventually reducing the unknown fields to just one. On the other hand, in a quasi-static scenario the dependence on time vanishes, and thus $\dot{\underline{u}} \approx \ddot{\underline{u}} \approx 0$. This makes it unnecessary to use a time integrator for solving the quasi-static motion problem, for $\underline{u}$ remains its only unknown. The resulting independence from t implies that quasi-static evolutions are nothing but a sequence of problems whose only mutual dependence resides in the irreversibility of α.

5. Preamble for the case studies of unstable crack propagation

The two following sections aim at developing the findings from Section 3 through detailed analyses based on the PFM and bespoke experiments on 3D printed specimens. For the sake of simplicity and representativeness, both simulated and real specimens were loaded under quasi-static displacement control yet ensuring unstable crack propagation. Furthermore, the studied geometries feature different interacting stress concentrators to replicate the aforementioned post-crack-onset interplay. In this sense, two different simulation strategies were pursued after crack onset: one quasi-static (QS) and one dynamic (DYN). For more details on the different resolution algorithms used, please refer to Appendix A.

The particular definitions of the PFM functions ψ, a and w correspond in what follows to the No Tension strain energy decomposition by Freddi and Royer-Carfagni (2010) and the AT1 phase field model (see e.g. De Lorenzis and Maurini, 2022). In turn, this results in a PFM wherein: (i) the damage field α can only develop in regions under tensile strain; (ii) purely elastic behavior is showcased far from the cracked regions (Marigo et al., 2016) thus better capturing the fracture energy component (Bleyer et al., 2017); and (iii) good agreement with other well-established criteria is obtained in the resulting size-effect of failure onset, even under complex stress states and multiaxial loadings (Chao Correas et al., 2023). Anyhow, it should be noted that the findings presented hereafter are not exclusive to the modelling choices above. For the sake of simplicity, bidimensional plane strain conditions were used for all subsequent simulations.

For a plane strain implementation of the PFM that combines the No Tension energy decomposition with the AT1 model, the resultant plain tensile strength σ_C depends on the magnitudes E, ν, G_C and ℓ through Eq. (33) (Chao Correas et al., 2023). As a consequence, ℓ was kept fixed and considered just as any other material property.

$$\sigma_C = \sqrt{\frac{3G_C E(1-\nu)}{8\ell(1+\nu)(1-2\nu)}} \tag{33}$$

With regard to the Finite Element simulations, first order triangular elements were used with an overall size equal to $\ell/4$ in order to properly capture the evolution of α in the cracked regions. Moreover, no localized mesh refinement was used so as to minimize, in the

dynamic simulations, any undesired wave reflections arising from the relatively higher stiffness of coarse elements. The same uniformly fine discretization was also used for the quasi-static simulations in order to avoid any mesh-related distortion in the comparison with the dynamic predictions.

The material properties and modelling parameters are reported in Table 1. These correspond to representative values characterizing the elastic and ultimate behavior of the Formlabs® Clear Resin used for the experiments. It being a photoreactive and methacrylated thermoset resin, cross-linking is triggered by photo-exposure. Therefore, controlling the passage of a moving laser beam over a region of interest allows for selective polymerization. By then repeating this process layer by layer, the desired solid component is generated through the process known as Stereolithography (SLA). Behavior-wise, the resulting polymer is similar to others used for fracture testing such as the PMMA, and it also showcases strong softening at loads close to fracture (which is mostly brittle, on the other hand). In an attempt to reduce the non-linear behavior, the UV+heating post-print curing process was performed at 75°C for 60 min per the findings by Marin et al. (2021). In any case, only qualitative comparisons between experiments and simulations were herein pursued; extensive material characterization campaigns or more precise but complex constitutive relations are thereby out of scope in the present work.

All the experiments were conducted using a DEBEN® Microtest 5 kN tensile stage (see Fig. 3) with a crosshead velocity of 1 mm/min so as to ensure global quasi-static conditions. The maximum thickness of the specimens is limited to approximately 4 mm, meaning that no actual plane strain specimens can be used. Still, since the experimental validation of the simulations is only qualitative, it is deemed acceptable to carry out the experiments on samples 4 mm thick.

The temporal evolution of the load exerted on each specimen was determined through the machine's built-in loadcell, while the specimen's elongation was captured through an in-house developed virtual extensometer which determines, via digital image processing, the relative position of two colored markers adhered to the specimen at the ends of the gauge section. This technique allows to eliminate the distortion from the elongation measurements due to the specimen sliding in the clamps, which is of special importance given the smallness of the specimens. Precision in the elongation readings was found to be of the order of microns.

6. Case study on the specimen type A: evidencing the kinetic energy contribution to the unstable development of fracture

The first of the two geometries herein studied is the so-called specimen type A depicted in Fig. 4, in which a rectangular domain features two different stress concentrators: a U-notch and a circular hole aligned. As a consequence, the specimen critical section is composed of two ligaments that interact upon fracture propagation akin to what preliminarily studied in Section 3. The motivation behind the chosen geometry is twofold: (i) the finiteness and smoothness of both stress concentrators result in high modelling and manufacturing accuracy; and (ii) the failure sequence is theoretically well-defined and predictable. This latter feature results essential for rigorously comparing the quasi-static and dynamic resolutions.

For the case at hand, the crack is expected to nucleate from the tip of the notch when $U_t = U_{C1}^{\{QS,\ DYN\}}$, in what will be hereafter called primal crack onset (see Fig. 5(a)). Immediately after, unstable crack propagation takes place along the first ligament up to the circular hole, yielding another U-notch just longer and with radius R. From here, a secondary crack onset event eventually occurs at $U_t = U_C^{\{QS,\ DYN\}}$ (see Fig. 5(b)), which can be either equal to or larger than $U_{C1}^{\{QS,\ DYN\}}$. In a first approximation, this depends on whether the stress concentrator of the newly formed U-notch is more severe than the original one. The two competing factors are the notch length and its tip radius: longer notches lead to more severe stress concentrators, whereas blunter tips have the opposite effect. Therefore, R determines the hole crack-stopping capability, and the bigger the R, the larger the energetic barrier for crack growth. As a consequence, a parametric analysis on the specimen type A with R as the only free parameter will show two differentiated failure regimes, i.e. one in which the elongations corresponding to primal, $U_{C1}^{\{QS,\ DYN\}}$, and secondary, $U_C^{\{QS,\ DYN\}}$, crack onsets are equal (Regime I), and one where the latter is higher (Regime II).

The dependence on R of the critical elongations at failure according to the quasi-static PFM, i.e. U_{C1}^{QS} and U_C^{QS}, is reported as the frontiers between specimen states in the chart of Fig. 6(a). Such figure must be read vertically from bottom to top: for each iso$R$ line, it indicates how the states of the corresponding specimen evolves as U_t grows. Thereof, the existence of two differentiated failure regimes depending on R results clear, with the transition occurring at $R_*^{QS} \approx 0.675$ mm. For $R \leq R_*^{QS}$, quasi-static simulations predict that the hole is not able to halt crack propagation, thereby showcasing a Regime I failure, i.e. $U_{C1}^{QS} = U_C^{QS}$. For $R > R_*^{QS}$ instead, the crack stopping capability of the hole becomes large enough to cause failure in Regime II, i.e. $U_{C1}^{QS} < U_C^{QS}$. In such cases, U_C^{QS} shows to be approximately proportional to a decimal root of R, this being consistent with findings on the size-effect of failure from U-notches (see e.g. Gómez et al., 2006). On the other hand, the analogous dynamic predictions are given in Fig. 6(b). The two failure regimes can be once again individuated, but in this case the transition occurs at a threshold considerably larger than before, with $R_*^{DYN} \in (1.75\ \text{mm},\ 2.0\ \text{mm})$. Noteworthy, the dynamic approach foresees the change of failure regime to take place abruptly, as opposed to the continuity showcased by its quasi-static counterpart.

The main reason behind this difference resides in the energetic transformations occurring during crack propagation according to each resolution technique. Taking $R = 1.5$ mm for instance, the quasi-static PFM predicts the energetic evolution as reported in Figs. 7.

Table 1
Material properties and modelling parameters used for the PFM simulations.

ρ [kg/m^3]	E [MPa]	ν [−]	G_C [N/mm]	σ_C [MPa]	ℓ [mm]
1180	2800	0.35	0.4	65	0.16

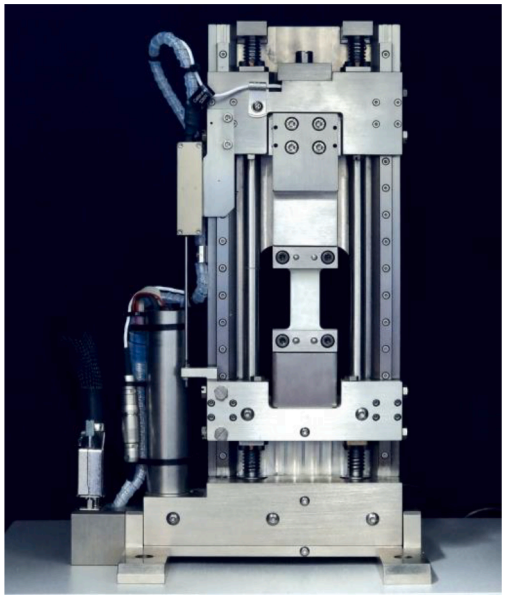


Fig. 3. DEBEN® Microtest 5 kN tensile stage used for testing the 3D printed specimens.

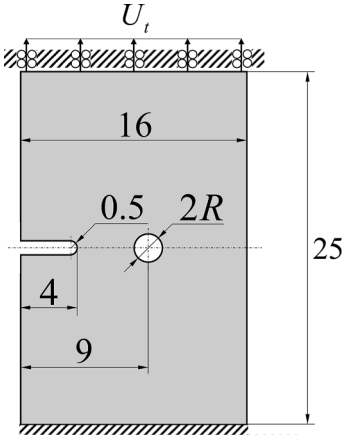


Fig. 4. Geometrical definition of the specimen type A. Dimensions in millimeters.

In particular, Fig. 7(a) shows linear elastic behavior with virtually no fracture energy component $\mathscr{E}_{\text{frac}}$ for $U_t < U_{C1}^{QS}$, this being followed by primal crack onset and complete breakage of the first ligament at $U_t = U_{C1}^{QS}$. Since the quasi-static approach does not explicitly follow unstable crack propagation, fracture "develops" within the AltMin scheme for each given time step. In this regard, Fig. 7(b) shows how the system energy components evolve with the AltMin iterations when $U_t = U_{C1}^{QS}$. Therein, as the crack "propagates" along the first ligament, $\mathscr{E}_{\text{frac}}$ increases and $\mathscr{E}_{\text{str}}$ decreases. Nonetheless, these two variances not being balanced causes the system potential energy $\mathscr{E}_{\text{str}} + \mathscr{E}_{\text{frac}}$ to diminish by almost 30 % once the crack has reached the hole. At that point, the system no longer has enough strain energy stored to overcome the hole energetic barrier, and crack propagation is halted. Further specimen elongation is required in order to reach the stored energy "threshold" for the secondary crack onset (and complete failure) to occur. This eventually takes place at $U_t = U_C^{QS}$, and is described in Fig. 7(c). Finally, all the system energy remains as $\mathscr{E}_{\text{frac}}$ but for a small component of $\mathscr{E}_{\text{str}}$ due to the numerically-required residual stiffness.

As expected, quasi-static PFM results showcase the well-known *snap-back* phenomenon. Such an occurrence is commonly studied by introducing an artificial control mechanism that is able to extract the excess of potential energy released from the system, thereby enabling quasi-static equilibrium conditions (see e.g. Carpinteri, 1989). This can be effectively achieved by controlling the crack mouth opening displacement or the crack extension itself. Nonetheless, the adoption of such control mechanisms alters the actual mechanical configuration by stabilizing the otherwise unstable crack growth, hence changing the setup of the modelled system with respect to that actually under study.

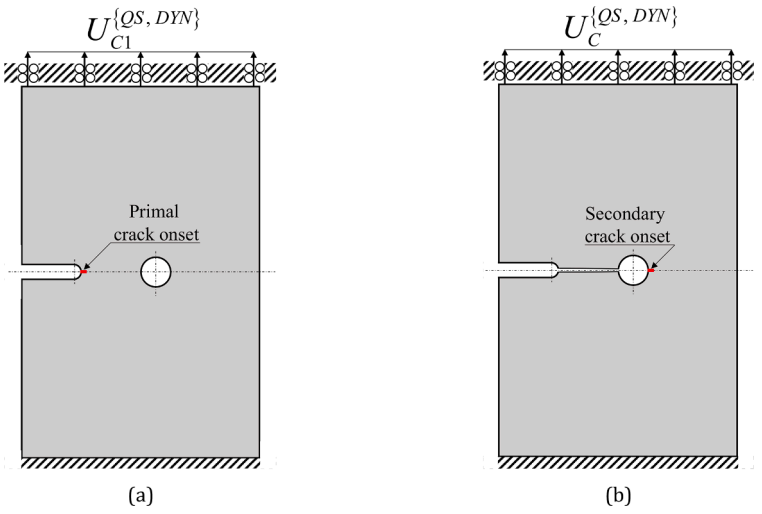


Fig. 5. Schematic representation of the specimen type A state at (a) primal and (b) secondary crack onset.

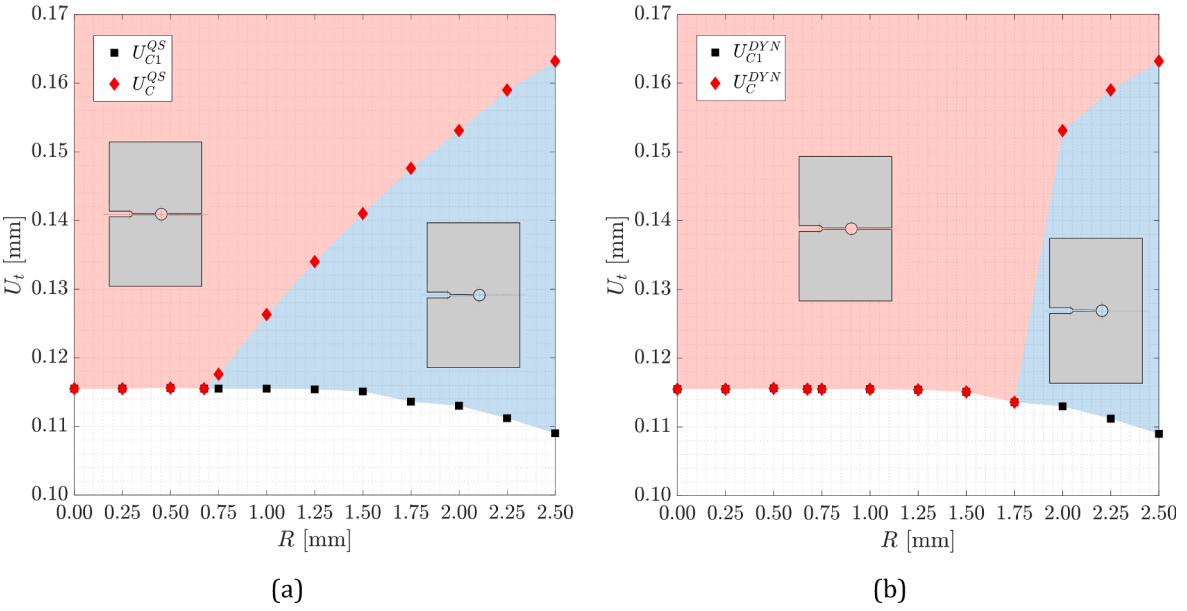


Fig. 6. Failure state map for the specimen type A according to: (a) the quasi-static and (b) the dynamic PFM.

A less intrusive line of action consists instead in enforcing dynamic equilibrium, thus converting the aforementioned surplus into kinetic energy and so conserving the total energy of the system. According to Larsen et al. (2010), the dynamic PFM does fulfil the total energy balance for vanishing time steps, a feature coherent with what is shown in Figs. 8 for $R = 1.5$ mm. For the sake of comparison, Fig. 8(a) is the counterpart of Fig. 7(a), whereas Fig. 8(b) is somewhat analogous to Figs. 7(b) and (c), yet now the X-axis represents the temporal coordinate of the dynamic evolution (see Appendix A).

As expected from Figs. 6, the dynamic PFM predicts failure in Regime I for $R = 1.5$ mm, and thus only one crack propagation event is reported in Fig. 8(a) at $U_t = U_{C1}^{DYN} = U_{C}^{DYN}$. The energetic transformations in Fig. 8(b) show that, since the total energy is (mostly) conserved, the reduction in potential energy as the crack propagates entails a matching increase in the kinetic energy. The key difference with respect to the quasi-static resolution manifests shortly after the crack has reached the circular hole, when the kinetic energy so far built up starts to partially transform back into strain energy (from $t \approx 11.8$ μs in Fig. 8b). Such a partial recovery is what eventually allows the system to overcome the energetic barrier for crack propagation associated to the hole, and to resume its breakage into the second ligament with no further specimen elongation.

Furthermore, the cases herein studied also revealed that even when both quasi-static and dynamic approaches predict failure in Regime II, the latter yields larger values for α at the site of secondary crack onset right after crack halt. This difference can be also

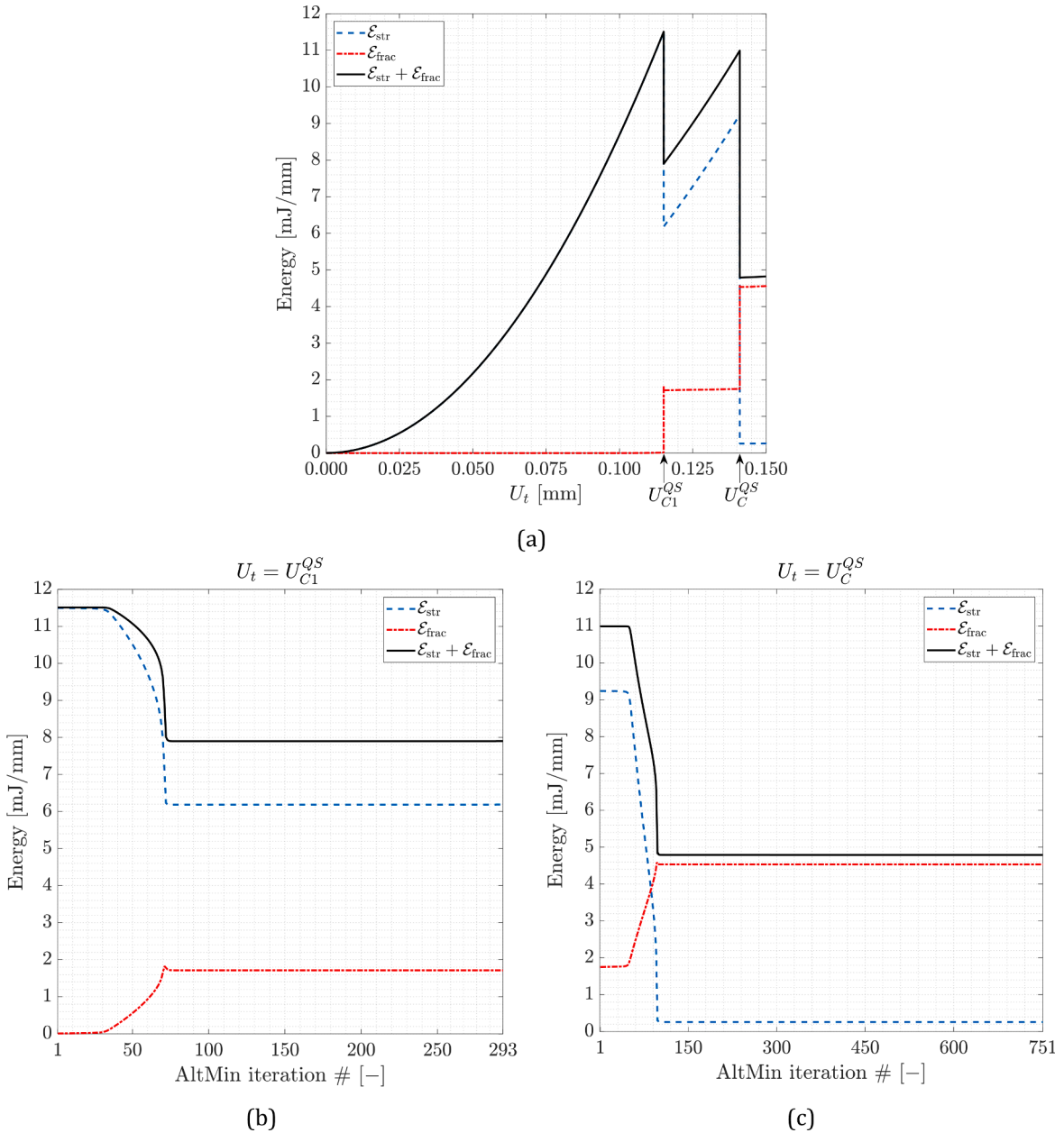


Fig. 7. Evolution of the energetic components along the fracture process of a specimen type A with $R = 1.5$ mm according to the quasi-static PFM.

attributed to the back-conversion from kinetic to strain energy, which despite not being large enough to trigger secondary crack onset, can still cause α to grow therein. In any case, U_C^{QS} and U_C^{DYN} were found to be virtually identical for those cases. This latter observation is coherent with what reported by Vieira de Carvalho et al. (2024) for the instability of a cohesive-modelled crack in a cantilever specimen perforated with an array of relatively large circular holes.

6.1. *Experimental results*

The experimental campaign directly compared the multi-ligament failure behavior with a quasi-static characterization of the hole energetic barrier. To that end, two main groups of specimens with constant R were tested: one featuring both ligaments (see Fig. 5a), and another in which the first ligament is already broken (see Fig. 5b). Besides that, specimens of both categories are identical. Therefore, if the former specimens break in Regime I at a smaller elongation than the latter, it would demonstrate that the dynamic effects upon unstable crack propagation are non-negligible.

A total of twelve specimens type A with a nominal hole radius $R = 0.5$ mm were 3D printed in the first place. The overall domain

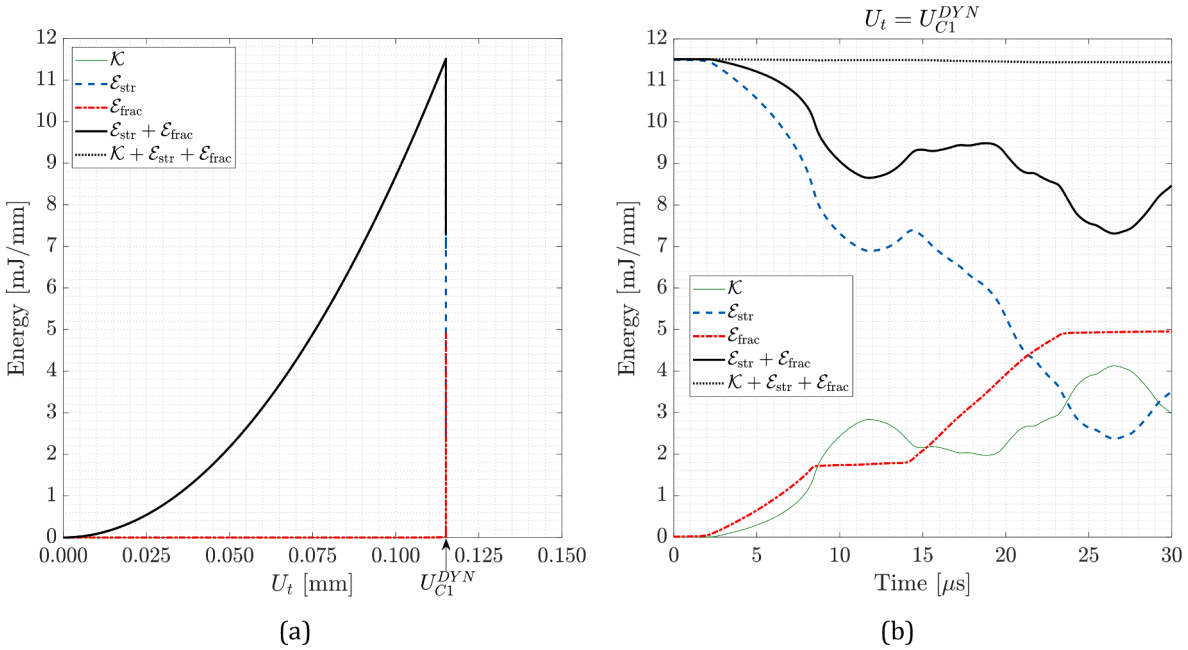


Fig. 8. Evolution of the energetic components along the fracture process of a specimen type A with $R = 1.5$ mm according to the dynamic PFM.

length of 25 mm herein corresponds to the distance between the barycenters of the two optical markers placed at the extremes of the gauge length (see Fig. 9). Preliminary experiments showed that the combination of manufacturing-related surface defects with the resin's high brittleness and complex behavior meant that fracture was no longer ensured to onset from the U-notch as desired. In order to avoid performing as many post mortem analyses as possible, the expected fracturing sequence was guaranteed instead by performing a slight cut at the tip of the U-notch with a razor blade. This is equivalent to reduce the effective radius of the U-notch, or somewhat to increasing the hole size while keeping the original notch.

Quantification of the effective notch radius reduction was done by comparing the ultimate behavior of two-ligament specimens without (type A) and with the cut (type A1), testing four specimens of each kind. Representativeness of the former's failure mode was checked by post-mortem analyses. The obtained experimental results for the ultimate elongation U_C^{EXP} and load F_C^{EXP} are reported in Tables 2 and 3, which yield an incision-caused reduction in the ultimate force by a factor 3.17 on average. Then using a maximum stress criterion and the U-notch stress field expression by Creager and Paris (1967), one can estimate the effective notch radius after the cut to be approximately 0.28 mm. Therefore, specimens type A1 are somewhat equivalent to the simulations with $R = 1.75$ mm from



Fig. 9. Video frame of a specimen type A1 with $R = 0.5$ mm (nominal) showing the digital recognition of the green (upper) and red (lower) optical markers. Each cross represents a marker barycenter.

Section 6, in the sense that they both have approximately the same ratio of radii between the effective notch and the hole.

Lastly, the remaining four specimens tested comprise another control group in which only the second ligament was load-bearing (type A2). The corresponding results reported in Table 4 unequivocally show, alongside those in Table 3, that specimens type A1 show failure in Regime I despite their ultimate elongation and force being considerably smaller than those of type A2. Hence, this empirically proves what has already been shown theoretically, i.e. that dynamic effects upon unstable crack propagation are significant even under quasi-static loading conditions.

7. Case study on the specimen type B: revealing the importance of progressive and sequential propagation of information

Another key aspect that is herein considered is how each model deals with the propagation of mechanical information within a continuum. Actually, such information diffuses through waves travelling at the speed of sound in the considered material $c \propto \sqrt{E/\rho}$, meaning that every evolving problem is dynamic in nature. Nonetheless, if and only if mechanical changes occur at slow enough rates, inertial effects can be then neglected and predictive models can be setup in a simplified quasi-static framework. Such an admissibility condition is, however, not commonly met for unstable fracture conditions since crack tip velocities are often of the order of magnitude of c.

Particularly, quasi-static frameworks disregard the concept of time, thereby leading to models where the mechanical information is instantaneously transmitted. Hence, every arbitrarily far location is assumed to become aware of and react to changes in the system configuration as they occur. Specifically for the case of unstable fracture, this results in the whole domain modifying its state of deformation as the crack evolves, which also affects subsequent crack growth and deformation states. In reality, by the time unstable fracture nucleates, only the surroundings of the newly formed crack receive notice of its growth and start to react accordingly. Therefore, a non-negligible difference exists between the quasi-statically predicted states and those physically admissible according to the diffusion of mechanical information.

The importance of such an issue will be herein studied using the specimen type B shown in Fig. 10, which results from modifying a specimen type A with $R = 1.5$ mm by vertically separating the notch and the hole by a distance H. The interaction between the two stress concentrators is now more intricate, and the prospective crack patterns are no longer trivial. In such regard, one can preemptively foresee a crack that propagates almost horizontally from the notch to then veer towards the hole progressively. Only for small enough values of H the crack can reach the hole, and the competition between halting or resuming propagation takes place; otherwise, the crack misses the hole and a single cracking event occurs. Such a behavioral difference depends on the crack ability to change direction, which is in turn determined by how it interacts with the hole as it propagates. As a consequence, any delays in the modelled transmission of mechanical information will manifest as less pronounced changes of direction. Therefore, differences in this regard have the potential to change whether the crack impinges the hole or not in an otherwise identical model.

For the case at hand, such a fundamental difference in the crack patterns predicted by the quasi-static and dynamic PFM was observed for $H = 2.5$ mm as shown in Fig. 11. Besides this, it is noteworthy how the quasi-static PFM surprisingly foresees straight cracks in contrast with the curviness obtained when dynamic effects are considered. Further analysis on the underlying reality of such an unexpected prediction reveals perhaps the biggest inconsistency of quasi-static approaches upon unstable cracking: the weakening of the crucial irreversibility condition of fracture.

As presented in Section 2, the quasi-static PFM seeks local minimization of the system's potential energy subjected to an irreversibility condition on α so that it can only grow pointwise with t. Such a restriction is only enforced with respect to previous converged states though, so that evolutions on α occurring within the AltMin scheme for a given time step are not irreversible. However, this leads to a paradox: the quasi-static PFM is allowed to "correct" the crack patterns obtained in past AltMin iterations within the same time step, yet based on information that is only generated after such states have been reached.

This line of reasoning is proven in Figs. 12, which report the crack patterns at different AltMin iterations of the time step in which the crack propagates along the first ligament, i.e. $U_t = U_{C1}^{QS}$. From Figs. 12(a) and (b) it is seen that until the crack reaches the circular hole, its path is curved and close to what initially expected. This confirms that the state of deformation drives the crack to propagate as such prior to entering the hole. Once the first ligament breaks completely however, the curved crack virtually yields the same decrease of $\mathscr{E}_{\text{str}}$ as if straight, yet it is more energetically expensive in terms of $\mathscr{E}_{\text{frac}}$. At the same time, the irreversibility condition is therein enforced with respect to the previous converged state, which was essentially pristine. As a consequence, subsequent AltMin iterations pursue the straightening of the crack along the first ligament, as clear from Figs. 12(b) through (d), so as to reduce the system's potential energy (see the complementary Fig. 13). The oxymoron is clear: the straight crack is energetically favorable once the first ligament is broken, but the deformation state drives fracture through a curved path from the notch to the hole. Therefore, given that fracture is irreversible, the straight crack solution can only be achieved by violating the cause-effect clause.

Table 2
Experimental results for the specimens type A.

	Specimen #				Overalls	
	1	2	3	4	Avg.	CoV %
$U_{C,A}^{EXP}$ [mm]	0.30	0.35	0.35	0.42	0.36	13.70
$F_{C,A}^{EXP}$ [N]	1540.3	1806.6	1727.9	1983.6	1764.6	10.42

Table 3
Experimental results for the specimens type A1.

	Specimen #				Overalls	
	1	2	3	4	Avg.	CoV %
$U^{EXP}_{C,\,A1}$ [mm]	0.07	0.09	0.11	0.08	0.09	19.00
$F^{EXP}_{C,\,A1}$ [N]	477.7	577.4	600.7	570.0	556.7	9.73

Table 4
Experimental results for the specimens type A2.

	Specimen #				Overalls	
	1	2	3	4	Avg.	CoV %
$U^{EXP}_{C,\,A2}$ [mm]	0.45	0.36	0.43	0.30	0.39	17.59
$F^{EXP}_{C,\,A2}$ [N]	984.4	779.8	996.3	761.2	880.4	14.45

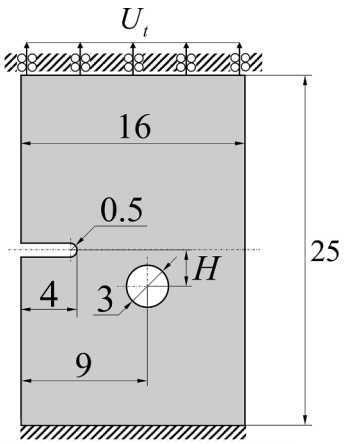


Fig. 10. Geometrical definition of the specimen type B. Dimensions in millimeters.

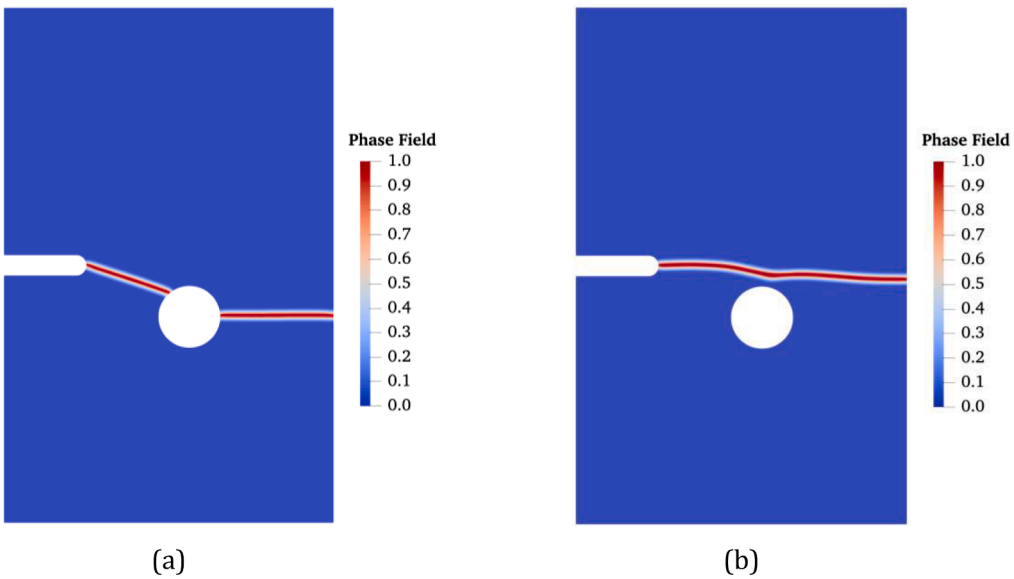


Fig. 11. Crack patterns for a specimen type B with $H = 2.5$ mm according to: (a) the quasi-static and (b) the dynamic PFM.

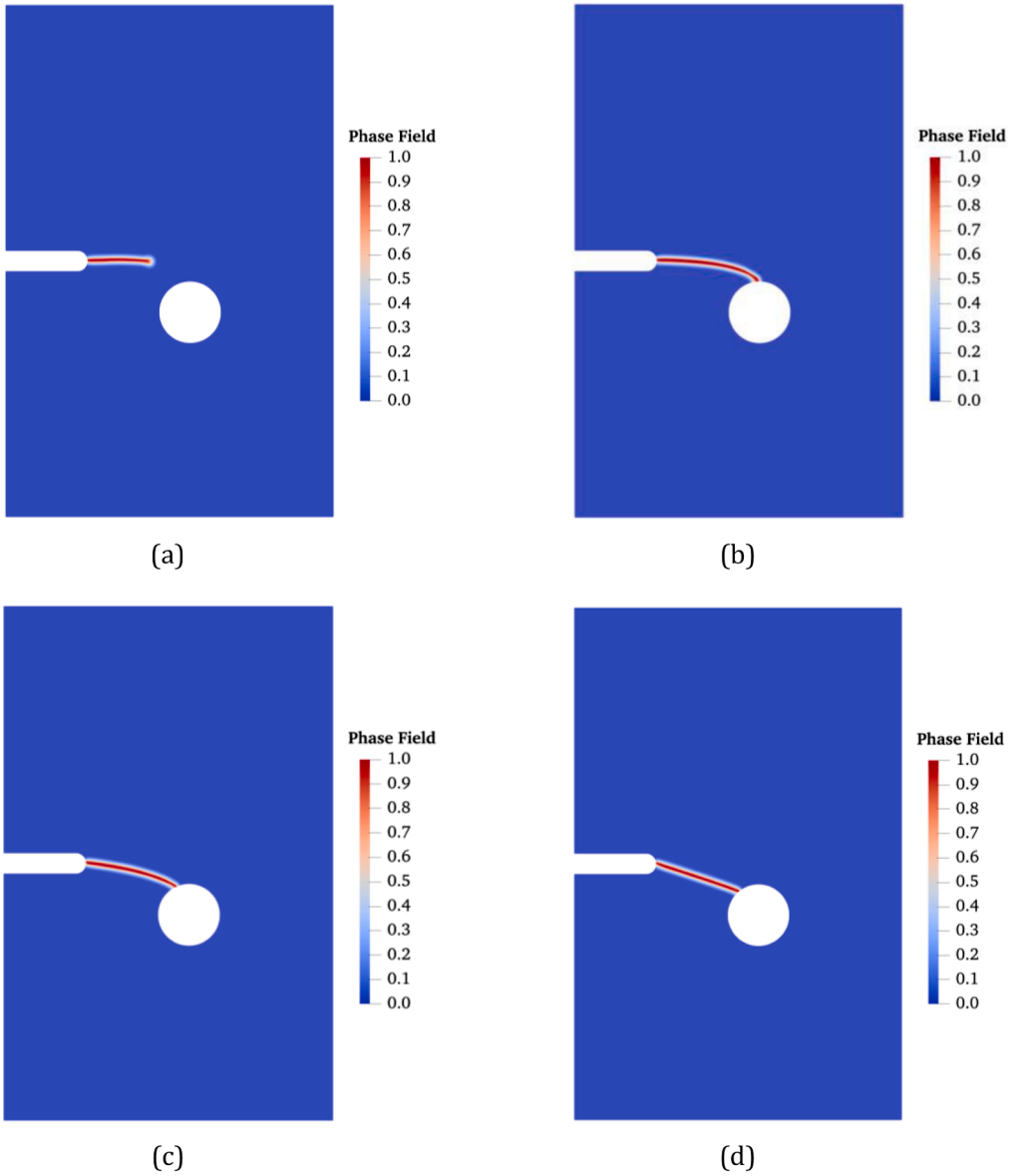


Fig. 12. Cracking of the first ligament in a specimen type B with $H = 2.5$ mm as resulting from the quasi-static PFM after (a) 100, (b) 500, (c) 1500 and (d) 4500 AltMin iterations.

7.1. Experimental results

Despite the fact that the theoretical discussion above is self-contained and robust, one can also present supporting experimental evidence. In such regard, one single specimen type B with $H = 2.5$ mm akin to the one simulated via PFM was manufactured and tested. As for the reasons discussed in Section 6.1, a slight cut was performed at the tip of the U-notch with a razor blade. Remarkably, the experimentally obtained crack pattern shown in Fig. 14(a) is curved and almost identical to the one obtained via dynamic PFM. This becomes evident in Fig. 14(b), where the predicted and actual crack patterns are superimposed.

8. Conclusions

The present investigation theoretically and empirically proves that the baseline hypotheses of quasi-static variational approaches for fracture are violated under unstable crack propagation, even under quasi-static loading conditions. Therefore, neglecting the inertial effects leads to flawed and potentially unsafe predictions, as demonstrated by a simplified Spring-Mass system for multi-ligament fracture. Such a preliminary model allowed identifying two main and mutually interrelated characteristics of quasi-static frameworks

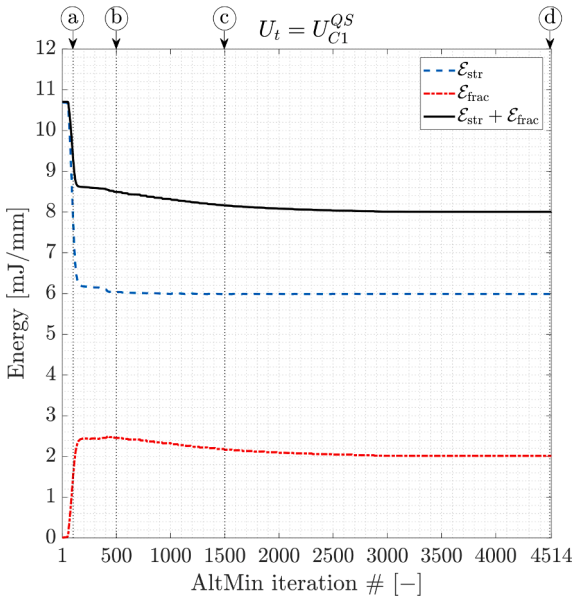


Fig. 13. Evolution with the AltMin iterations of the energetic components for the fracturing of the first ligament of a specimen type B with $H = 2.5$ mm according to the quasi-static PFM. Bullet notes on top indicate correspondence with Figs. 12.

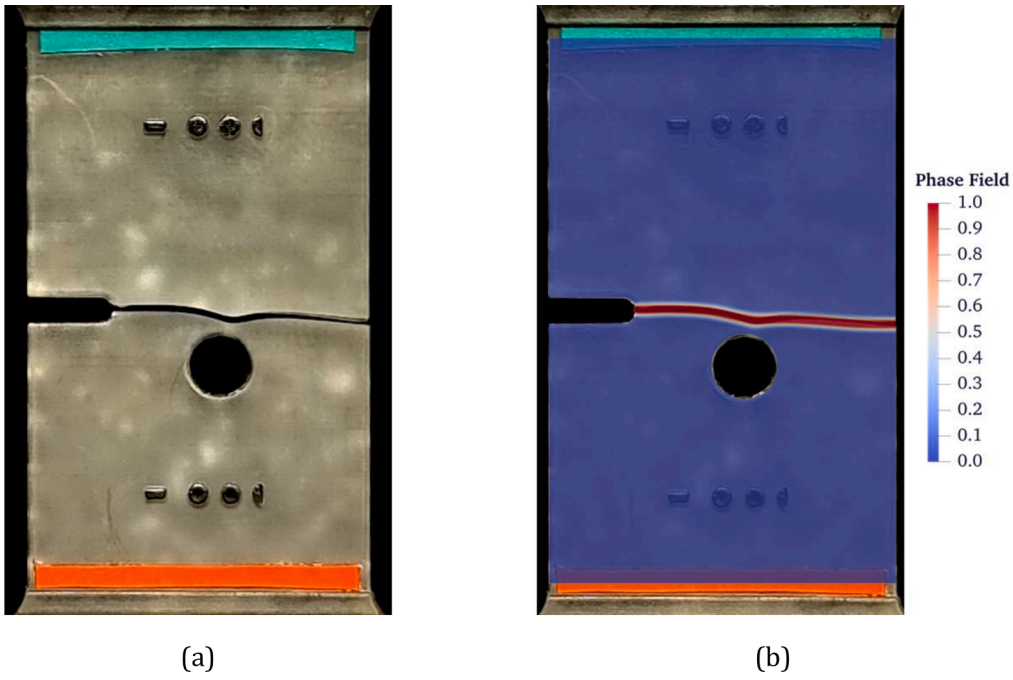


Fig. 14. (a) Picture of the experimental crack pattern of a specimen type B with $H = 2.5$ mm, and (b) superimposition of the predictions by the dynamic PFM.

that render the resultant fracture predictions non-representative: (i) the neglection of the kinetic energy component, and (ii) the immediateness in the propagation of mechanical information.

Based on these preliminary observations, two different case studies were designed to highlight each one of the two points above. To that end, the well-established Phase Field fracture model was chosen for it is able to cope nicely with bulk fracture, and both quasi-static and dynamic variants are available. Likewise, the theoretical results are backed by experimental results from tests conducted on bespoke 3D printed specimens. From the detailed case studies, three main conclusions can be drawn:

- The paradigm of local minimization of the potential energy causes quasi-static approaches to predict an unrealistic dissipation of energy for unstable fractures. Commonly known as the snap-back phenomenon when under displacement control, most of this energy surplus is not actually lost but transformed into kinetic energy. This can then partially transform back into strain energy, further fueling crack propagation in the presence of energetic barriers and rendering quasi-static predictions potentially unsafe.
- Assuming quasi-static equilibrium for rapidly developing events involves deeming states as admissible despite being unphysical per requiring the mechanical information to travel faster than the continuum speed of sound. Such an assumption undermines the representativeness of the resultant crack patterns and the foreseen behavior upon unstable fracture.
- The inability of quasi-static approaches to explicitly follow unstable crack propagation considerably weakens the robustness of the crucial irreversibility condition for fracture, leading to the acceptance of solutions that violate the cause-effect clause.

Finally, one should consider that none of the inconsistencies found in the quasi-static predictions are exclusive to the Phase Field fracture model but are common to most variational approaches to fracture. This, combined with the widespread occurrence of unstable fracture in real structures, even under quasi-static loading conditions, underscore the importance of the obtained results.

CRediT authorship contribution statement

A. Chao Correas: Conceptualization, Software, Writing – original draft, Visualization. **J. Reinoso:** Conceptualization, Writing – review & editing. **P. Cornetti:** Conceptualization, Writing – review & editing. **M. Corrado:** Conceptualization, Writing – review & editing, Supervision.

Declaration of competing interest

The authors declare that they have no known competing financial interests or personal relationships that could have appeared to influence the work reported in this paper.

Data availability

Data will be made available on request.

Acknowledgements


This project has received funding from the European Union's Horizon 2020 research and innovation programme under the Marie Skłodowska Curie grant agreement No 861061.

J. Reinoso appreciates the support from the European Union Horizon 2020 research and innovation program under the Marie Skłodowska-Curie Grant Agreement No. 101086342- Project DIAGONAL>(Ductility and fracture toughness analysis of Functionally Graded Materials: HORIZON-MSCA-2021-SE-01 action).

J. Reinoso is grateful to Ministerio de Ciencia e Innovación de España (Project TED2021–131649B-I00).

Appendix A. Kernels of the PFM resolution algorithms

The algorithms for the resolution kernels of the quasi-static and the dynamic PFM approaches are provided as Algorithm A1 and Algorithm A2, respectively. It is to be noted that fields in italic represent the mathematical forms, i.e. expressions that are not discretized in the Finite Element (FE) context, while magnitudes in bold represent the discretized fields. Clearly, the formers need to be discretized for its FE implementation in any case, but the form notation is retained wherever possible because it is more generic. Eventually, for a problem with N degrees of freedom, $\mathbf{1}$ represents a $N \times 1$ vector whose components are equal to 1, whereas $\mathbf{I}$ is the $N \times N$ identity matrix.

Algorithm A1
Kernel of the resolution algorithm for the quasi-static PFM problem using the staggered approach with an AltMin scheme.

(*continued on next page*)

Algorithm A1 (*continued*)

Initialize $\left\{t,\ \Delta t,\ i,\ N_{\text{fails}},\ \underline{u}_{t_0},\ \alpha_{t_0}\right\} \leftarrow \left\{t_0,\ \Delta t_0,\ 1,\ 0,\ \underline{u}_0,\ \alpha_0\right\}$
Repeat while $t_i \leq T$ and $N_{\text{fails}} \leq N_{\text{fails_max}}$:
  Update Dirichlet BCs on $\underline{u}$ and α to t_i
  Set $\left\{j,\ \text{converged},\ \underline{u}_{i\,0},\ \alpha_{i\,0}\right\} \leftarrow \left\{0,\ \text{False},\ \underline{u}_{t_{i-1}},\ \alpha_{t_{i-1}}\right\}$
  Repeat while $j \leq N_{\text{iter_max}}$ and converged is False:
    Update $j \leftarrow j+1$
    Solve for $\underline{u}_{ij}$ with $\alpha = \alpha_{ij-1}$ fixed
    Solve for α_{ij} with $\underline{u} = \underline{u}_{ij}$ fixed
    Assess converged for $\left(\underline{u}_{ij},\ \alpha_{ij}\right)$
  If converged is True:
    Assign $\left\{\underline{u}_{t_i},\ \alpha_{t_i}\right\} \leftarrow \left\{\underline{u}_{ij},\ \alpha_{ij}\right\}$
    Determine Δt
    Perform postprocessing
    Update $t_{i+1} \leftarrow t_i + \Delta t$
    Update $i \leftarrow i+1$
    Set $N_{\text{fails}} \leftarrow 0$
  Else:
    Set $t_i \leftarrow \tau$ with $\tau \in (t_{i-1},\ t_i)$
    Update $N_{\text{fails}} \leftarrow N_{\text{fails}} + 1$

Algorithm A2
Kernel of the resolution algorithm for the dynamic PFM problem using an explicit time integration scheme based on the Newmark's β-method.

Initialize $\left\{t,\ i,\ \underline{u}_{t_0},\ \underline{\dot{u}}_{t_0},\ \underline{\ddot{u}}_{t_0},\ \alpha_{t_0}\right\} \leftarrow \left\{t_0,\ 1,\ \underline{u}_0,\ \underline{\dot{u}}_0,\ \underline{\ddot{u}}_0,\ \alpha_0\right\}$
Determine Δt according to Courant–Friedrichs–Lewy condition
Compute the consistent mass matrix $\mathbf{M}$
Compute the lumped mass matrix $\mathbf{M_L} \leftarrow (\mathbf{M}\ \mathbf{1})\ \mathbf{I}$
Repeat while $t_{i+1} \leq T$:
  Update Dirichlet BCs on $\underline{u}$, $\underline{\dot{u}}$, $\underline{\ddot{u}}$ and α to t_{i+1}
  Propagate $\underline{u}$ to t_{i+1}: $\underline{u}_{t_{i+1}} \leftarrow \underline{u}_{t_i} + \Delta t\,\underline{\dot{u}}_{t_i} + \Delta t^2 \underline{\ddot{u}}_{t_i}\,/2$
  Impose restricted DoFs of $\underline{u}_{t_{i+1}}$ per the Dirichlet BCs on $\underline{u}$
  Solve for $\alpha_{t_{i+1}}$ with $\underline{u} = \underline{u}_{t_{i+1}}$ fixed
  Compute the motion stiffness matrix $\mathbf{K_u}(\alpha_{t_{i+1}})$
  Compute the vector of nodal forces $\mathbf{F}_{t_{i+1}} \leftarrow -\,\mathbf{K_u}(\alpha_{t_{i+1}})\ \mathbf{u}_{t_{i+1}}$
  Propagate $\underline{\ddot{u}}$ to t_{i+1}: $\ddot{\mathbf{u}}_{t_{i+1}} \leftarrow \mathbf{M_L}^{-1}\ \mathbf{F}_{t_{i+1}}$
  Correct restricted DoFs of $\underline{\ddot{u}}_{t_{i+1}}$ per the Dirichlet BCs on $\underline{\ddot{u}}$
  Propagate $\underline{\dot{u}}$ to t_{i+1}: $\underline{\dot{u}}_{t_{i+1}} \leftarrow \underline{\dot{u}}_{t_i} + \Delta t\left(\underline{\ddot{u}}_{t_{i+1}} + \underline{\ddot{u}}_{t_i}\right)/2$
  Correct restricted DoFs of $\underline{\dot{u}}_{t_{i+1}}$ per the Dirichlet BCs on $\underline{\dot{u}}$
  Update $t_{i+1} \leftarrow t_i + \Delta t$
  Update $i \leftarrow i+1$

References

Albertini, G., Lebihain, M., Hild, F., Ponson, L., Kammer, D.S., 2021. Effective Toughness of Heterogeneous Materials with Rate-Dependent Fracture Energy. Phys. Rev. Lett. 127, 035501 https://doi.org/10.1103/PhysRevLett.127.035501.

Ambrosio, L., Tortorelli, V.M., 1990. Approximation of functional depending on jumps by elliptic functional via t-convergence. Commun. Pure Appl. Math. 43, 999–1036. https://doi.org/10.1002/cpa.3160430805.

Barenblatt, G.I., 1962. The Mathematical Theory of Equilibrium Cracks in Brittle Fracture, in: Advances in Applied Mechanics. pp. 55–129. https://doi.org/10.1016/S0065-2156(08)70121-2.

Bleyer, J., Molinari, J.F., 2017. Microbranching instability in phase-field modelling of dynamic brittle fracture. Appl. Phys. Lett. 110 https://doi.org/10.1063/1.4980064.

Bleyer, J., Roux-Langlois, C., Molinari, J.F., 2017. Dynamic crack propagation with a variational phase-field model: limiting speed, crack branching and velocity-toughening mechanisms. Int. J. Fract. 204, 79–100. https://doi.org/10.1007/s10704-016-0163-1.

Borden, M.J., Verhoosel, C.V., Scott, M.A., Hughes, T.J.R., Landis, C.M., 2012. A phase-field description of dynamic brittle fracture. Comput. Methods Appl. Mech. Eng. 217–220, 77–95. https://doi.org/10.1016/j.cma.2012.01.008.

Bourdin, B., Francfort, G.A., Marigo, J.J., 2008. The Variational Approach to Fracture. J. Elast. 91, 5–148. https://doi.org/10.1007/s10659-007-9107-3.

Bourdin, B., Francfort, G.A., Marigo, J.J., 2000. Numerical experiments in revisited brittle fracture. J. Mech. Phys. Solids 48, 797–826. https://doi.org/10.1016/S0022-5096(99)00028-9.

Bourdin, B., Larsen, C.J., Richardson, C.L., 2011. A time-discrete model for dynamic fracture based on crack regularization. Int. J. Fract. 168, 133–143. https://doi.org/10.1007/s10704-010-9562-x.

Camacho, G.T., Ortiz, M., 1996. Computational modelling of impact damage in brittle materials. Int. J. Solids Struct. 33, 2899–2938. https://doi.org/10.1016/0020-7683(95)00255-3.

Carpinteri, A., 1989. Cusp catastrophe interpretation of fracture instability. J. Mech. Phys. Solids 37, 567–582. https://doi.org/10.1016/0022-5096(89)90029-X.
Cavuoto, R., Lenarda, P., Misseroni, D., Paggi, M., Bigoni, D., 2022. Failure through crack propagation in components with holes and notches: An experimental assessment of the phase field model. Int. J. Solids Struct. 257, 111798 https://doi.org/10.1016/j.ijsolstr.2022.111798.
Chao Correas, A., Sapora, A., Reinoso, J., Corrado, M., Cornetti, P., 2023. Coupled versus energetic nonlocal failure criteria: A case study on the crack onset from circular holes under biaxial loadings. Eur. J. Mech. - A/Solids, 105037. https://doi.org/10.1016/j.euromechsol.2023.105037.
Corrado, M., Paggi, M., Reinoso, J., 2022. Dynamic formulation of phase field fracture in heterogeneous media with finite thickness cohesive interfaces. Comput. Mater. Sci. 205, 111226 https://doi.org/10.1016/j.commatsci.2022.111226.
Creager, M., Paris, P.C., 1967. Elastic field equations for blunt cracks with reference to stress corrosion cracking. Int. J. Fract. Mech. 3, 247–252. https://doi.org/10.1007/BF00182890.
De Lorenzis, L., Maurini, C., 2022. Nucleation under multi-axial loading in variational phase-field models of brittle fracture. Int. J. Fract. 237, 61–81. https://doi.org/10.1007/s10704-021-00555-6.
Dugdale, D.S., 1960. Yielding of steel sheets containing slits. J. Mech. Phys. Solids 8, 100–104. https://doi.org/10.1016/0022-5096(60)90013-2.
Francfort, G.A., Marigo, J.J., 1998. Revisiting brittle fracture as an energy minimization problem. J. Mech. Phys. Solids 46, 1319–1342. https://doi.org/10.1016/S0022-5096(98)00034-9.
Freddi, F., Royer-Carfagni, G., 2010. Regularized variational theories of fracture: A unified approach. J. Mech. Phys. Solids 58, 1154–1174. https://doi.org/10.1016/j.jmps.2010.02.010.
Gómez, F.J., Guinea, G.V., Elices, M., 2006. Failure criteria for linear elastic materials with U-notches. Int. J. Fract. 141, 99–113. https://doi.org/10.1007/s10704-006-0066-7.
Griffith, A.A., 1921. VI. The phenomena of rupture and flow in solids. Philos. Trans. R. Soc. London. Ser. A, Contain. Pap. a Math. or Phys. Character 221, 163–198. https://doi.org/10.1098/rsta.1921.0006.
Hofacker, M., Miehe, C., 2013. A phase field model of dynamic fracture: Robust field updates for the analysis of complex crack patterns. Int. J. Numer. Methods Eng. 93, 276–301. https://doi.org/10.1002/nme.4387.
Inglis, C.E., 1913. Stresses in Plates Due to the Presence of Cracks and Sharp Corners. Trans. Inst. Nav. Archit. 55, 219–241.
Larsen, C.J., Ortner, C., Süli, E., 2010. Existence of solutions to a regularized model of dynamic fracture. Math. Model. Methods Appl. Sci. 20, 1021–1048. https://doi.org/10.1142/S0218202510004520.
Laschuetza, T., Seelig, T., 2021. Remarks on dynamic cohesive fracture under static pre-stress — With a comparison to finite fracture mechanics. Eng. Fract. Mech. 242, 107466 https://doi.org/10.1016/j.engfracmech.2020.107466.
Li, T.Y., Marigo, J.J., Guilbaud, D., Potapov, S., 2016. Gradient damage modeling of brittle fracture in an explicit dynamics context. Int. J. Numer. Methods Eng. 108, 1381–1405. https://doi.org/10.1002/nme.5262.
Li, T.Y., Marigo, J.J., Guilbaud, D., Potapov, S., 2015. Variational Approach to Dynamic Brittle Fracture via Gradient Damage Models. Appl. Mech. Mater. 784, 334–341. https://doi.org/10.4028/www.scientific.net/AMM.784.334.
Marigo, J.J., Maurini, C., Pham, K., 2016. An overview of the modelling of fracture by gradient damage models. Meccanica 51, 3107–3128. https://doi.org/10.1007/s11012-016-0538-4.
Marin, E., Boschetto, F., Zanocco, M., Doan, H.N., Sunthar, T.P.M., Kinashi, K., Iba, D., Zhu, W., Pezzotti, G., 2021. UV-curing and thermal ageing of methacrylated stereo-lithographic resin. Polym. Degrad. Stab. 185, 109503 https://doi.org/10.1016/j.polymdegradstab.2021.109503.
Miehe, Christian, Hofacker, M., Welschinger, F., 2010. A phase field model for rate-independent crack propagation: Robust algorithmic implementation based on operator splits. Comput. Methods Appl. Mech. Eng. 199, 2765–2778. https://doi.org/10.1016/j.cma.2010.04.011.
Miehe, C., Welschinger, F., Hofacker, M., 2010. Thermodynamically consistent phase-field models of fracture: Variational principles and multi-field FE implementations. Int. J. Numer. Methods Eng. 83, 1273–1311. https://doi.org/10.1002/nme.2861.
Negri, M., Ortner, C., 2008. Quasi-static crack propagation by Griffith's criterion. Math. Model. Methods Appl. Sci. 18, 1895–1925. https://doi.org/10.1142/S0218202508003236.
Pham, K., Amor, H., Marigo, J.J., Maurini, C., 2011. Gradient Damage Models and Their Use to Approximate Brittle Fracture. Int. J. Damage Mech. 20, 618–652. https://doi.org/10.1177/1056789510386852.
Sargado, J.M., Keilegavlen, E., Berre, I., Nordbotten, J.M., 2018. High-accuracy phase-field models for brittle fracture based on a new family of degradation functions. J. Mech. Phys. Solids 111, 458–489. https://doi.org/10.1016/j.jmps.2017.10.015.
Schlüter, A., Willenbücher, A., Kuhn, C., Müller, R., 2014. Phase field approximation of dynamic brittle fracture. Comput. Mech. 54, 1141–1161. https://doi.org/10.1007/s00466-014-1045-x.
Tian, F., Zeng, J., Tang, X., Xu, T., Li, L., 2020. A dynamic phase field model with no attenuation of wave speed for rapid fracture instability in hyperelastic materials. Int. J. Solids Struct. 202, 685–698. https://doi.org/10.1016/j.ijsolstr.2020.07.004.
Vieira de Carvalho, M., Rodrigues Lopes, I.A., Andrade Pires, F.M., 2024. On the solution of unstable fracture problems with non-linear cohesive laws. Eng. Fract. Mech. 295, 109736 https://doi.org/10.1016/j.engfracmech.2023.109736.
Vocialta, M., Corrado, M., Molinari, J.F., 2018. Numerical analysis of fragmentation in tempered glass with parallel dynamic insertion of cohesive elements. Eng. Fract. Mech. 188, 448–469. https://doi.org/10.1016/j.engfracmech.2017.09.015.
Wu, J.Y., 2017. A unified phase-field theory for the mechanics of damage and quasi-brittle failure. J. Mech. Phys. Solids 103, 72–99. https://doi.org/10.1016/j.jmps.2017.03.015.
Zhou, F., 1996. Study On the Macroscopic Behavior and the Microscopic Process of Dynamic Crack Propagation. The University of Tokyo.